JASA ARTICLE

Numerical study of the coupling layer between transducer and chip in acoustofluidic devices[a)]

William Naundrup Bodé[b)] and Henrik Bruus[c)]
Department of Physics, Technical University of Denmark, Danmarks Tekniske Universitet Physics Building 309, Kongens Lyngby, DK-2800, Denmark

ABSTRACT:
By numerical simulation in two and three dimensions, the coupling layer between the transducer and microfluidic chip in ultrasound acoustofluidic devices is studied. The model includes the transducer with electrodes, microfluidic chip with a liquid-filled microchannel, and coupling layer between the transducer and chip. Two commonly used coupling materials, solid epoxy glue and viscous glycerol, as well as two commonly used device types, glass capillary tubes and silicon-glass chips, are considered. It is studied how acoustic resonances in ideal devices without a coupling layer are either sustained or attenuated as a coupling layer of increasing thickness is inserted. A simple criterion based on the phase of the acoustic wave for whether a given zero-layer resonance is sustained or attenuated by the addition of a coupling layer is established. Finally, by controlling the thickness and the material, it is shown that the coupling layer can be used as a design component for optimal and robust acoustofluidic resonances.
 https://doi.org/10.1121/10.0004871
(Received 29 January 2021; revised 13 April 2021; accepted 16 April 2021; published online 6 May 2021)
[Editor: James F. Lynch] Pages: 3096–3105

I. INTRODUCTION

The acoustic impedance matching techniques for piezoelectric (PZT) sensors and transducers is, in general, a well-studied field as exemplified by the recent review by Rathod.[1] However, specifically for ultrasound acoustofluidic devices, the role of the coupling layer (also known as the carrier or matching layer) between the transducer and microfluidic chip remains poorly understood beyond one-dimensional (1D) planar systems.[2,3] Whereas the function of a matching layer for 1D traveling waves through layered structures is simply to couple acoustic energy more efficiently into subsequent layers, its role in resonant 1D acoustofluidic systems is less straightforward. As analyzed by Glynne-Jones *et al.*,[3] the function of the coupling layer may be more structural to isolate the transducer from the fluid layer. In the present work, we study the more complex case of a fully three-dimensional (3D) acoustofluidic system.

Extending the numerical study by Hahn and Dual, given for one specific device with a 20-μm-thick epoxy glue coupling layer,[4] we present 3D numerical simulations of a PZT transducer coupled to an acoustofluidic chip through a thin coupling layer of varying thickness, consisting of either a solid glue or viscous liquid. We consider two commonly used types of acoustofluidic devices sketched in Fig. 1, glass capillary tubes and silicon-glass chips. Capillary-tube devices have been applied as acoustic particle traps, relying on a small transducer that actuates a vertical resonant pressure mode locally in the capillary.[5–8] Silicon-glass devices have been applied for continuous-flow focusing and separation of particle suspensions, relying on the bulk actuation of horizontal resonance modes in embedded microchannels.[9–11]

The paper is organized as follows. In Sec. II, we present the basic theory, including governing equations and boundary conditions. In Sec. III, we model the capillary-tube particle traps and show their dependency on the coupling-layer thickness. In Sec. IV, a similar analysis is carried out for the conventional acoustophoresis silicon-glass devices. Finally, in Sec. V, we present a concluding discussion regarding the criterion established in Secs. III and IV for designing acoustofluidic devices with acoustic resonance modes that are relatively insensitive to the thickness of the coupling layer.

II. THEORY AND MODEL ASSUMPTIONS

In establishing the numerical model, we closely follow the theory presented by Skov *et al.*[12] Our model consists of a lead-zirconate-titanate PZT transducer coupled to an elastic solid, which contains the fluid-filled microchannel. Theoretically, the system is described by three continuous fields: the electric potential φ in the PZT transducer, the mechanical displacement field $\boldsymbol{u}$ in the elastic solid and the PZT transducer, and the acoustic pressure p_1 in the fluid. The coupling layer is described by p_1 if it is a liquid and $\boldsymbol{u}$ if it is a solid. Due to the linearity of the governing equations, all fields have a harmonic time dependence $\mathrm{e}^{-\mathrm{i}\omega t}$ with an angular frequency $\omega = 2\pi f$ and frequency f. Thus, a given field has the structure $\tilde{f}(\boldsymbol{r},t) = f(\boldsymbol{r})\,\mathrm{e}^{-\mathrm{i}\omega t}$, and we need only

[a)]This paper is part of a special issue on Theory and Applications of Acoustofluidics.
[b)]Electronic mail: bruus@fysik.dtu.dk, ORCID: 0000-0002-7014-0127.
[c)]ORCID: 0000-0001-5827-2939.

https://doi.org/10.1121/10.0004871

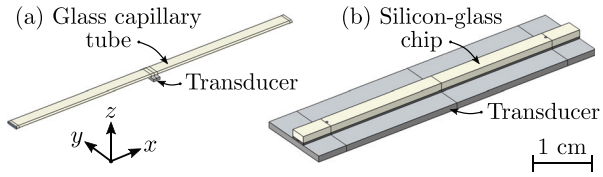

FIG. 1. (Color online) Sketch of the two types of acoustofluidic devices considered in this study. (a) A glass capillary tube (beige) mounted on a small PZT transducer (gray) and (b) a silicon-glass chip (black base, beige lid) mounted on a large PZT transducer (gray). The sketches are drawn to scale.

determine the complex-valued space-dependent amplitude $f(\boldsymbol{r})$.

The acoustic pressure field p_1 is modeled using the effective pressure acoustic theory by Bach and Bruus,[13] where the viscous boundary layers are included analytically in the effective boundary conditions. Using the effective theory, the acoustic pressure p_1 in a fluid with density ρ_0, sound speed c_0, dynamic viscosity η_0, and bulk viscosity η^b is governed by the Helmholtz equation, and the acoustic velocity $\boldsymbol{v}_1$ is proportional to $\boldsymbol{\nabla} p_1$,

$$\nabla^2 p_1 = -k_c^2 p_1, \quad \boldsymbol{v}_1 = -\mathrm{i}\frac{1-\mathrm{i}\Gamma}{\omega\rho_0}\boldsymbol{\nabla} p_1, \tag{1a}$$

with

$$k_0 = \frac{\omega}{c_0}, \quad k_c = \left(1+\frac{\mathrm{i}}{2}\Gamma\right)k_0, \tag{1b}$$

and

$$\Gamma = \left(\frac{\eta^b}{\eta_0}+\frac{4}{3}\right)\frac{\omega\eta_0}{\rho_0 c_0^2}. \tag{1c}$$

In cases in which the fluid coupling-layer thickness Δ is comparable or smaller than the viscous boundary-layer length scale $\delta_{\mathrm{visc}} = \sqrt{2\eta_0/(\rho_0\omega)}$, the effective theory fails, and the full perturbation model is used instead.[14,15]

The mechanical displacement field $\boldsymbol{u}$ is governed by the linear Cauchy equation, involving the stress tensor $\boldsymbol{\sigma}$,

$$-\rho_0\omega^2\boldsymbol{u} = \boldsymbol{\nabla}\cdot\boldsymbol{\sigma}. \tag{2}$$

The components σ_{ik} of $\boldsymbol{\sigma}$ are related to the strain components $\frac{1}{2}(\partial_i u_k + \partial_k u_i)$ by the stiffness tensor $\boldsymbol{C}$, which, for linear isotropic or cubic-symmetric elastic materials, are written in the Voigt notation as

$$\begin{pmatrix}\sigma_{xx}\\ \sigma_{yy}\\ \sigma_{zz}\\ \hline \sigma_{yz}\\ \sigma_{xz}\\ \sigma_{xy}\end{pmatrix} = \left(\begin{array}{ccc|ccc} C_{11} & C_{12} & C_{12} & 0 & 0 & 0\\ C_{12} & C_{11} & C_{12} & 0 & 0 & 0\\ C_{12} & C_{12} & C_{11} & 0 & 0 & 0\\ \hline 0 & 0 & 0 & C_{44} & 0 & 0\\ 0 & 0 & 0 & 0 & C_{44} & 0\\ 0 & 0 & 0 & 0 & 0 & C_{44}\end{array}\right) \times \begin{pmatrix}\partial_x u_x\\ \partial_y u_y\\ \partial_z u_z\\ \hline \partial_y u_z + \partial_z u_y\\ \partial_x u_z + \partial_z u_x\\ \partial_x u_y + \partial_y u_x\end{pmatrix}. \tag{3}$$

Mechanical damping is implemented as complex-valued elastic moduli, defined as $C_{ik} = (1-\mathrm{i}\Gamma_{\mathrm{sl}})c_{ik}$. In the PZT transducer, the electric potential φ is governed by the quasi-static Gauss equation, involving the electric displacement $\boldsymbol{D}$,

$$\boldsymbol{\nabla}\cdot\boldsymbol{D} = 0. \tag{4}$$

Furthermore, in PZT, the complete linear electromechanical coupling relating the stress and electric displacement to the strain and electric field is given by the Voigt notation as

$$\begin{pmatrix}\sigma_{xx}\\ \sigma_{yy}\\ \sigma_{zz}\\ \hline \sigma_{yz}\\ \sigma_{xz}\\ \sigma_{xy}\\ \hline D_x\\ D_y\\ D_z\end{pmatrix} = \left(\begin{array}{ccc|ccc|ccc} C_{11} & C_{12} & C_{13} & 0 & 0 & 0 & 0 & 0 & -e_{31}\\ C_{12} & C_{11} & C_{13} & 0 & 0 & 0 & 0 & 0 & -e_{31}\\ C_{13} & C_{13} & C_{33} & 0 & 0 & 0 & 0 & 0 & -e_{33}\\ \hline 0 & 0 & 0 & C_{44} & 0 & 0 & 0 & -e_{15} & 0\\ 0 & 0 & 0 & 0 & C_{44} & 0 & -e_{15} & 0 & 0\\ 0 & 0 & 0 & 0 & 0 & C_{66} & 0 & 0 & 0\\ \hline 0 & 0 & 0 & 0 & e_{15} & 0 & \varepsilon_{11} & 0 & 0\\ 0 & 0 & 0 & e_{15} & 0 & 0 & 0 & \varepsilon_{11} & 0\\ e_{31} & e_{31} & e_{33} & 0 & 0 & 0 & 0 & 0 & \varepsilon_{33}\end{array}\right) \begin{pmatrix}\partial_x u_x\\ \partial_y u_y\\ \partial_z u_z\\ \hline \partial_y u_z + \partial_z u_y\\ \partial_x u_z + \partial_z u_x\\ \partial_x u_y + \partial_y u_x\\ \hline -\partial_x\varphi\\ -\partial_y\varphi\\ -\partial_z\varphi\end{pmatrix}. \tag{5}$$

A. Acoustic energy density

Throughout this study, the time- and volume-averaged acoustic energy density E_{ac} in the water-filled channel is used as a measure and indicator of how the acoustic resonances are affected by the coupling layer. In a fluid volume V, the averaged acoustic energy density is given as

$$E_{\mathrm{ac}} = \frac{1}{V}\int\left(\frac{1}{4}\rho_0|\boldsymbol{v}_1|^2 + \frac{1}{4}\kappa_0|p_1|^2\right)\mathrm{d}V. \tag{6}$$

B. Boundary conditions

At the fluid–solid interface, the boundary conditions are no-slip and continuous stress, together with zero stress on the free surfaces. Introducing the mechanical displacement velocity $\boldsymbol{v}_{\mathrm{sl}} = -\mathrm{i}\omega\boldsymbol{u}$ and a shear wave number $k_s = (1+\mathrm{i})/\delta_{\mathrm{visc}}$, the effective continuous velocity and stress boundary conditions become[13]

$$\boldsymbol{n}\cdot\boldsymbol{v}_1 = \boldsymbol{n}\cdot\boldsymbol{v}_{\mathrm{sl}} + \frac{\mathrm{i}}{k_s}\nabla_{\parallel}\cdot(\boldsymbol{v}_{\mathrm{sl}} - \boldsymbol{v}_1), \tag{7a}$$

$$\boldsymbol{\sigma}\cdot\boldsymbol{n} = -p_1\boldsymbol{n} + \mathrm{i}k_s\eta_0\left(\boldsymbol{v}_{\mathrm{sl}} + \frac{\mathrm{i}}{\omega\rho_0}\nabla p_1\right), \tag{7b}$$

where the unit vector $\boldsymbol{n}$ is the outward surface normal from the solid domain. In experiments, the electrical signal is driven by a sine-wave function generator coupled to the transducer electrodes. This setup is implemented as a constant-potential boundary condition on the electrode–transducer interface. Furthermore, we assume no free charges, which is implemented as a zero flux condition on the electric displacement field $\boldsymbol{D}$. In the 3D capillary-tube device, symmetries are exploited such that the full system can be reduced to one-quarter. The boundary conditions are listed in Table I. Except for the symmetry conditions, the same boundary condition applies for the silicon-glass device.

C. Unbounded perfectly matched layers

For long systems like the capillary tubes, a no-reflection boundary condition can be established closer to the origin of the domain by using the perfectly matched layer (PML) technique, thus, reducing the computational domain substantially. It involves a complex coordinate transformation of the form $x \to x + (\mathrm{i}/\omega)\int^x\theta(x')\,\mathrm{d}x'$, such that outgoing waves are attenuated within a distance comparable to the wavelength. The PML technique requires a choice of damping function θ, and we adopt the one from Bermúdez *et al.*[16]

TABLE I. List of the boundary conditions used in the modeled acoustofluidic systems. The unit vector $\boldsymbol{n}$ is the surface outward normal with respect to the solid domain, and $\boldsymbol{t}$ is any of the two tangential unit vectors. $V_0 = 1$ V.

Domain ← boundary	Boundary condition
Solid domain ← air	$\boldsymbol{\sigma}\cdot\boldsymbol{n} = \boldsymbol{0}$
Fluid domain ← solid	Eq. (7a)
Solid domain ← fluid	Eq. (7b)
Fluid domain ← air	$p_1 = 0$
PZT domain ← bottom electrode	$\varphi = 0$
PZT domain ← top electrode	$\varphi = V_0$
Solid domain ← symmetry	$\boldsymbol{u}\cdot\boldsymbol{n} = 0,\ \boldsymbol{t}\cdot\boldsymbol{\sigma}\cdot\boldsymbol{n} = 0$
Fluid domain ← symmetry	$\boldsymbol{n}\cdot\nabla p_1 = 0$

$$\theta(x) = \begin{cases} 0, & \text{for } x \le L_{\mathrm{cap}}, \\ \dfrac{\beta}{L_{\mathrm{pml}} - (x - L_{\mathrm{cap}})} - \dfrac{\beta}{L_{\mathrm{pml}}}, & \text{for } x > L_{\mathrm{cap}}. \end{cases} \tag{8}$$

The parameters defining $\theta(x)$ are chosen appropriately for a given system: L_{cap} is the position of the interface between the physical capillary tube and PML domain, L_{pml} is the length of the PML domain, and β is the damping strength. The axial coordinate x is complex valued for $x > L_{\mathrm{cap}}$ inside the PML domain. The function θ is classified as a continuous unbounded damping function, and it is effective in terms of numerical error and reflections at the PML interface $x = L_{\mathrm{cap}}$.[16]

D. Numerical implementation in COMSOL Multiphysics

The numerical model was implemented in the finite element software COMSOL Multiphysics[17] using "weak form PDE" in the mathematics module and closely following Ref. 12, where further implementation details can be found. The mesh settings are adopted from Ley and Bruus.[18] The scripts were computed on a workstation with a 12 core 3.5 GHz central processing unit (CPU) processor and 128 GB random access memory (RAM).

III. CAPILLARY-TUBE PARTICLE TRAPS

As the first example, we investigate the capillary-tube device that is widely used as a versatile acoustic trap in many experimental studies.[5–8] The corresponding model system is sketched in Fig. 2, indicating the different domains together with the PML layer and a zoom-in on the coupling layer. The dimensions and materials used in the numerical model are listed in Tables II and III, respectively. The model system is similar to the one studied by Ley and Bruus,[18] but now the model is extended to include a PZT transducer and coupling layer. Typically, the capillary-tube device is

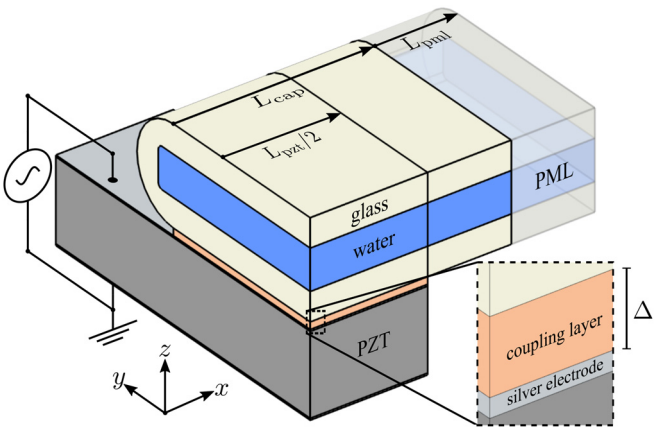

FIG. 2. (Color online) One-quarter of the capillary-tube-based model system with a zoom-in on the coupling layer of thickness Δ. The model system includes a water-filled glass capillary coupled to a PZT transducer with silver electrodes. The top electrode is coupled to a time-harmonic function generator and the bottom electrode is grounded.

https://doi.org/10.1121/10.0004871

TABLE II. The length (L), width (W), and height (H) of the glass capillary tube (cap), channel (ch), PZT transducer (pzt), and silver electrodes (el). The curvatures of the outer and inner rounded corners are 240 μm and 25 μm, respectively. The bottom ($H_{\mathrm{gl,bot}}$) and top ($H_{\mathrm{gl,top}}$) glass-wall thicknesses are both 140 μm.

Symbol	Value	Symbol	Value
L_{cap}	1573 μm	L_{ch}	1573 μm
W_{cap}	2280 μm	W_{ch}	2000 μm
H_{cap}	480 μm	H_{ch}	200 μm
L_{pzt}	1160 μm	L_{el}	1160 μm
W_{pzt}	3350 μm	W_{el}	3350 μm
H_{pzt}	400 μm	H_{el}	9 μm

characterized by having a standing half-wave-like resonance in the vertical direction. This is achieved with a PZT transducer having a predesigned mode at 5 MHz as used in preliminary experiments by the Laurell group at Lund University.

TABLE III. List of parameters used in the numerical simulations. Note that $C_{12} = C_{11} - 2C_{44}$ for the isotropic materials. Isotropy in the xy-plane implies $C_{66} = \frac{1}{2}(C_{11} - C_{12})$ for the PZT.

Parameter	Symbol	Value	Unit
Water at 25 °C (Ref. 19)			
Mass density	ρ_0	997.05	kg m^{-3}
Speed of sound	c_0	1496.7	m s^{-1}
Compressibility	κ_0	447.7	TPa^{-1}
Dynamic viscosity	η_0	0.890	mPa s
Bulk viscosity	η^{b}	2.485	mPa s
Isotropic Pyrex borosilicate glas (Ref. 20)			
Mass density	ρ_{sl}	2230	kg m^{-3}
Elastic modulus	c_{11}	69.7	GPa
Elastic modulus	c_{44}	26.2	GPa
Mechanical damping coeff.	Γ_{sl}	0.0004	—
Isotropic silver (Ref. 21)			
Mass density	ρ_{sl}	10 485	kg m^{-3}
Elastic modulus	c_{11}	133.9	GPa
Elastic modulus	c_{44}	25.9	GPa
Mechanical damping coefficient	Γ_{sl}	0.0004	—
Cubic-symmetric silicon (Ref. 22)			
Mass density	ρ_{sl}	2329	kg m^{-3}
Elastic modulus	c_{11}	165.7	GPa
Elastic modulus	c_{44}	79.6	GPa
Elastic modulus	c_{12}	63.9	GPa
Mechanical damping coefficient	Γ_{sl}	0.0001	—
Pz26 PZT ceramic (Refs. 4 and 23)			
Mass density	ρ_{sl}	7700	kg m^{-3}
Elastic modulus	c_{11}	168	GPa
Elastic modulus	c_{12}	110	GPa
Elastic modulus	c_{13}	99.9	GPa
Elastic modulus	c_{33}	123	GPa
Elastic modulus	c_{44}	30.1	GPa
Coupling constant	e_{15}	9.86	C/m^2
Coupling constant	e_{31}	−2.8	C/m^2
Coupling constant	e_{33}	14.7	C/m^2
Electric permittivity	ε_{11}	828	ε_0
Electric permittivity	ε_{33}	700	ε_0
Mechanical damping coefficient	Γ_{sl}	0.02	—

A. The specific PML

We implement no-reflection boundary conditions using a PML layer with parameter values $\beta = 2c_{\mathrm{lo}}^{(\mathrm{gl})} = 11.294$ m/s and $L_{\mathrm{pml}} = 413$ μm. The superscript refers to the material, in this case, glass (gl), and $c_{\mathrm{lo}}^{(\mathrm{gl})}$ and $\lambda_{\mathrm{lo}}^{(\mathrm{gl})}$ are the longitudinal sound speed and wavelength, respectively. The numerical error introduced by using the PML is shown in Fig. 3 in terms of the convergence parameter C, which for a given field solution g is defined by

$$C(g) = \sqrt{\frac{\int |g - g_{\mathrm{ref}}|^2 \mathrm{d}V}{\int |g_{\mathrm{ref}}|^2 \mathrm{d}V}}, \tag{9}$$

where g_{ref} is a reference solution. The integration domain is taken as the transducer region for $x \le L_{\mathrm{pzt}}/2$ as defined in Fig. 2. In Fig. 3, the error measure C is evaluated at six different geometries at a fixed frequency $f = 3.84$ MHz with $\lambda_{\mathrm{lo}}^{(\mathrm{gl})} = 1.47$ mm. The reference solution is taken as $L_{\mathrm{cap}} = 1.35\lambda_{\mathrm{lo}}^{(\mathrm{gl})}$. We choose the system length $L_{\mathrm{cap}} = 1.07\lambda_{\mathrm{lo}}^{(\mathrm{gl})}$ such that the maximal numerical error due to the unbounded PML is estimated to be $C = 3 \times 10^{-4}$.

B. Coupling-layer analysis in 3D and 1D models

Continuing with the physics studies, we consider two coupling materials: a viscous mixture of 99% volume-per-volume (v/v) glycerol and 1% v/v water, and a solid ED-20 epoxy resin, which from now on will be referred to as glycerol and epoxy for brevity. The coupling material parameters used in the simulations are listed in Table IV.

In practice, the glycerol coupling allows for reuseability of the acoustofluidic chip and/or transducer, whereas the epoxy is used to ensure a well-defined but permanent coupling.[9,24–27] These layers are reported to have a thickness in the range from 5 to 20 μm.[6,7,28–31] Here, we investigate the effect of the coupling layer by calculating the resonances as a function of coupling-layer material and thickness Δ using the 3D model. For each coupling-layer thickness Δ, the

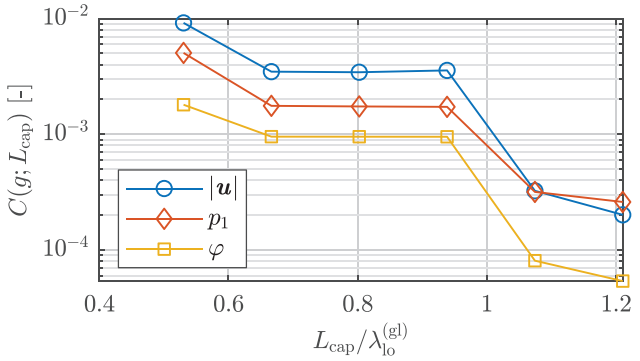

FIG. 3. (Color online) Numerical convergence C for $\boldsymbol{u}$, p_1, and φ in the PML of Fig. 2 at frequency $f_{\mathrm{res}} = 3.84$ MHz with wavelength $\lambda_{\mathrm{lo}}^{(\mathrm{gl})} = 1.47$ mm, PML length $L_{\mathrm{pml}} = 413$ μm, and the physical system length L_{cap} is varied as $L_{\mathrm{cap}}/\lambda_{\mathrm{lo}}^{(\mathrm{gl})} = 0.53, 0.67, 0.80, 0.94, 1.07$, and 1.21.

TABLE IV. List of the coupling layer parameters for glycerol (a 99% v/v glycerol and 1% v/v water mixture) and epoxy at 20 °C. The coefficient C_{12} of the epoxy is obtained through the relation $C_{12} = C_{11} - 2C_{44}$.

Parameter	Symbol	Value	Unit
Glycerol (Ref. 32–34)			
Mass density	ρ_{glc}	1260.4	kg m^{-3}
Speed of sound	c_{glc}	1922.8	m s^{-1}
Compressibility	κ_{glc}	214.6	TPa^{-1}
Dynamic viscosity	η_{glc}	1.137	Pa s
Bulk viscosity	$\eta^{\mathrm{b}}_{\mathrm{glc}}$	0.790	Pa s
Epoxy (Ref. 35)			
Mass density	ρ_{sl}	1205	kg m^{-3}
Elastic modulus	c_{11}	9.583	GPa
Elastic modulus	c_{44}	2.164	GPa
Mechanical damping coefficient	Γ_{sl}	0.01	—

average acoustic energy density E_{ac} in the water-filled channel is computed as a function of the frequency from 3.0 to 4.5 MHz. Resonances are then identified as peaks in the acoustic energy spectrum $E_{\mathrm{ac}}(f)$. The resonances are illustrated in the scatterplot of Fig. 4, where the points represent resonances at a frequency f for a coupling-layer thickness Δ in the range from 0 to 100 μm with point areas proportional to $E_{\mathrm{ac}}/E^0_{\mathrm{ac}}$, where E^0_{ac} is the acoustic energy density without a coupling layer. The Δ-independent resonance frequencies of the unloaded PZT resonances are plotted to indicate where the transducer is most active.

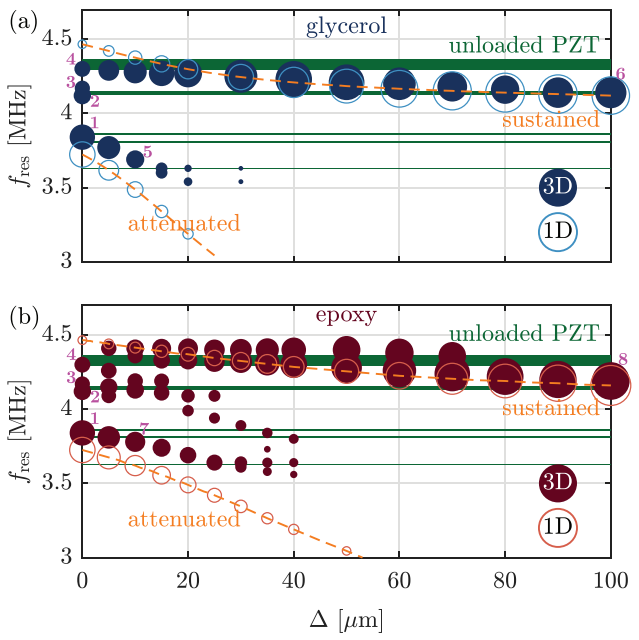

FIG. 4. (Color online) Resonance frequencies in the capillary-tube device as a function of increasing coupling-layer thickness Δ for (a) glycerol and (b) epoxy. The 3D and 1D model resonance frequencies are plotted as filled and empty circles, respectively, with an area proportional to $E_{\mathrm{ac}}/E^0_{\mathrm{ac}}$. The dashed lines represent the 1D resonance frequencies, indicating a sustained or attenuated behavior. The solid green lines indicate unloaded PZT resonances with a linewidth proportional to the logarithm of the acoustic energy density in the PZT. Animated gif-files of the eight modes enumerated 1–8 (magenta numbers) are given in the supplementary material (Ref. 36).

The 3D model reveals a distinct behavior for both glycerol and epoxy coupling layers: As the coupling layer Δ increases, one resonance is attenuated (E_{ac} decreases) and has a large downshift in frequency, whereas another is sustained (E_{ac} increases) and has a small downshift in frequency. This behavior is also observed in an idealized 1D layer model along the vertical z axis with seven domains: electrode, PZT, electrode, coupling layer, glass, water, glass of respective thicknesses H_{el}, H_{pzt}, H_{el}, Δ, $H_{\mathrm{gl,bot}}$, H_{ch}, and $H_{\mathrm{gl,top}}$. This 1D model takes into account only z-components, z-dependencies, densities, and longitudinal sound speeds in the governing equations. The 1D model resonances are plotted together with the 3D resonances in Fig. 4. Of course, Fig. 4 reveals that the 3D model exhibits more resonances than the 1D model due to the extended degrees of freedom in the transverse directions and shear waves.

In Fig. 4, we have selected eight 3D resonance modes enumerated 1–8 (magenta numbers). For each of these modes, we have computed an animated gif-file that shows the temporal behavior and is given in the supplementary material.[36] The five 3D resonance modes 1, 5, 6, 7, and 8, which are close to the 1D modes indicated by the orange-dashed lines in Fig. 4, indeed appear as 1D-like with a prominent standing wave in the vertical z-direction in the region above the transducer. This indicates that the attenuated and sustained resonance-mode effect represented by the 3D modes 1-5-7 and 6-8, respectively, can be explained by this 1D fluid-like model. The other three 3D resonance modes 2, 3, and 4, lying farther away from the 1D modes, have a more clear 3D nature with waves in all three spatial directions.

C. A design criterion for coupling layers

As the layer thickness Δ is changed from 0 to 100 μm, the sustaining and attenuating behaviors of the zero-layer resonances are elucidated by studying the pressure profiles for each of the resonances in the 1D model. For each profile, we choose a temporal phase factor $\mathrm{e}^{-\mathrm{i}\omega t}$ that gives the maximum *positive amplitude* in the PZT domain.

In Fig. 5(a), the 1D resonance pressure profiles are evaluated at three different epoxy coupling-layer thicknesses $\Delta = 0$, 20, and 50 μm for the sustained resonance. In Fig. 5(b), the same is shown for the attenuated resonance. Without the coupling layer, the fluid–solid interface is located at $z_0 = H_{\mathrm{pzt}} + 2H_{\mathrm{el}} + H_{\mathrm{gl,bot}} = 558$ μm and has a coupling layer at $z_\Delta = z_0 + \Delta$. As a result, the value of the pressure $p_1(z_\Delta)$ is decreasing. In Fig. 5(a), labeled "sustained," we have $p_1(z_\Delta) < p_1(z_0) < 0$, yielding an *increased magnitude* of the pressure as Δ is increased. In contrast, in Fig. 5(b), labeled "attenuated," we have $0 < p_1(z_\Delta) < p_1(z_0)$, yielding a *decreasing magnitude* of the pressure for increasing Δ. Clearly, if a given zero-layer resonance has a negative (positive) value of $p_1(z_0)$ for the specified temporal phase factor, the resonance is sustained (attenuated). The sign of $p_1(z_0)$ is determined by the accumulated spatial phase factor $\Phi(z_0)$ of the fluid-solid value $p_1(z_0)$ relative to the surface value

https://doi.org/10.1121/10.0004871

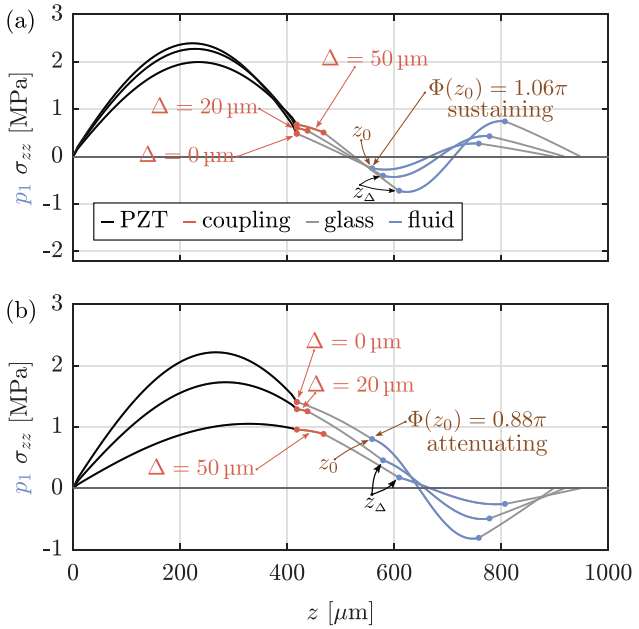

FIG. 5. (Color online) Plots of normal stress $\sigma_{zz}(z)$ and pressure $p_1(z)$ in the 1D model with an epoxy coupling layer for the three layer thicknesses $\Delta = 0$, 20, and 50 μm for (a) the sustained and (b) attenuated zero-layer resonance modes. The profiles are plotted at a phase where the amplitude is at a maximum. The accumulated phase Φ is calculated without a coupling layer at the fluid–solid interface at $z_0 = H_{\mathrm{pzt}} + 2H_{\mathrm{el}} + H_{\mathrm{gl,bot}}$ (brown arrow).

$p_1(0)$. In the 1D model, $\Phi(z_0)$ is given by the wave number k_i and layer thickness H_i of each layer (i = PZT, electrodes, and glass placed at $z < z_0$). Consequently, we arrive at the criterion

$$\text{sustaining coupling if } \Phi(z_0) > \pi, \tag{10a}$$

$$\text{attenuating coupling if } \Phi(z_0) < \pi, \tag{10b}$$

with

$$\Phi(z_0) = \sum_i k_i H_i = \sum_i \frac{\omega}{c_{\mathrm{lo}}^{(i)}} H_i. \tag{10c}$$

Note that this criterion is only valid for $|\Phi(z_0)| < \frac{3}{2}\pi$. For the given capillary-tube device, the values of $\Phi(z_0)$ for the sustained and attenuated zero-layer resonance are $3.32 = 1.06\pi$ and $2.77 = 0.88\pi$, respectively. The criterion [Eq. (10)] is an extension of previous 1D analyses[2,3] here shown to apply in a 3D analysis, and it is one of the main results of the paper. It can be used to design optimally coupled capillary devices with minimum attenuation caused by the coupling layer.

D. Characteristic coupling-layer attenuation thickness Δ_0

Based on the 1D model, we derive a semi-analytical estimate for the characteristic thickness Δ_0 at which the acoustic energy is attenuated for the abovementioned attenuated zero-layer resonance modes. The pressure solution $p_{1,i}$ to the Helmholtz equation in each domain i is written as

$$p_{1,i} = p_{a,i} \sin(k_i z + \phi_i) \quad \text{for } z \in \Omega_i. \tag{11}$$

At the interface between domain i and $i+1$, the acoustic pressure and velocity must be continuous,

$$p_{1,i+1} = p_{1,i}, \quad \frac{1}{\rho_{i+1}} \partial_z p_{1,i+1} = \frac{1}{\rho_i} \partial_z p_{1,i}. \tag{12}$$

This results in an iterative formula for the amplitude $p_{a,i}$ and phase ϕ_i with coefficients $\beta_{i+1,i}$, $a_{i+1,i}$, and $b_{i+1,i}$,

$$p_{a,i+1} = \beta_{i+1,i}\, p_{a,i}, \tag{13a}$$

$$\phi_{i+1} = \phi_i - k_{i+1} \sum_j^i H_j + \arctan(a_{i+1,i}/b_{i+1,i}), \tag{13b}$$

$$\beta_{i+1,i} = \sqrt{1 + \cos^2\left(k_i \sum_j^i H_j + \phi_i\right)(Z_{i+1,i}^2 - 1)}, \tag{13c}$$

$$a_{i+1,i} = \beta_{i+1,i}^{-1} \sin\left(k_i \sum_j^i H_j + \phi_i\right), \tag{13d}$$

$$b_{i+1,i} = \beta_{i+1,i}^{-1} Z_{i+1,i} \cos\left(k_i \sum_j^i H_j + \phi_i\right), \tag{13e}$$

$$Z_{i+1,i} = \frac{\rho_{i+1} c_{\mathrm{lo}}^{(i+1)}}{\rho_i c_{\mathrm{lo}}^{(i)}}. \tag{13f}$$

For a coupling layer (cl) made of either epoxy or glycerol, we have a mismatch $Z_{\mathrm{cl,pzt}} \ll 1$ in the acoustic impedance, and the pressure amplitude $p_1(z_0)$ at the interface z_0 can, therefore, be approximated as

$$p_1(z_0) \approx p_0 \sqrt{\alpha^2 + \beta^2} \sin(k_{\mathrm{cl}} H_{\mathrm{pzt}}) \times \sin(\arctan(\alpha/\beta) + k_{\mathrm{gl}} H_{\mathrm{gl}}) + \mathcal{O}(Z_{\mathrm{cl,pzt}}), \tag{14a}$$

with

$$\alpha = Z_{\mathrm{gl,cl}} \sin(k_{\mathrm{cl}}\Delta) \quad \text{and} \quad \beta = \cos(k_{\mathrm{cl}}\Delta). \tag{14b}$$

By further assuming $E_{\mathrm{ac}} \propto p_1^2(z_0)$ and $k_{\mathrm{cl}}^2 \Delta^2 \ll 1$, the lowest order functional dependence in the layer thickness Δ becomes

$$E_{\mathrm{ac}} \propto p_0^2 \sin^2(k_{\mathrm{cl}} H_{\mathrm{pzt}}) \left[\cos^2(k_{\mathrm{gl}} H_{\mathrm{gl}}) - Z_{\mathrm{gl,cl}} k_{\mathrm{cl}} \Delta \sin(2 k_{\mathrm{gl}} H_{\mathrm{gl}})\right]. \tag{15}$$

By setting $E_{\mathrm{ac}} = 0$, we extract the characteristic thickness scale Δ_0 at which the resonance is attenuated

$$\Delta_0 = \frac{Z_{\mathrm{cl,gl}} c_{\mathrm{lo}}^{(\mathrm{cl})}}{2\omega} \cot\left(\frac{\omega H_{\mathrm{gl}}}{c_{\mathrm{lo}}^{(\mathrm{gl})}}\right). \tag{16}$$

In Fig. 6, the normalized acoustic energy density $E_{\mathrm{ac}}(\Delta)/E_{\mathrm{ac}}^0$ is plotted as a function of the normalized coupling-layer

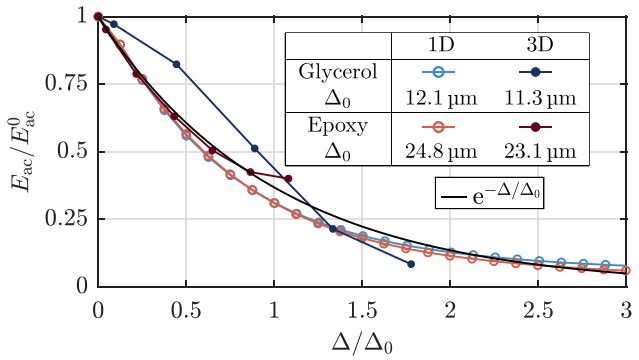

FIG. 6. (Color online) The normalized acoustic energy density E_{ac}/E^0_{ac} for the attenuated capillary-tube resonance versus the normalized coupling-layer thickness Δ/Δ_0 for glycerol and epoxy, simulated in the 3D and 1D models. The exponential function $e^{-\Delta/\Delta_0}$ (black) is inserted as a guide to the eye.

thickness Δ/Δ_0. The acoustic energy is seen to be attenuated on the length scale Δ_0 as predicted by Eq. (16) with $\Delta_0 = 12.1$ μm and 24.8 μm for glycerol and epoxy, respectively. For both coupling materials, we observe an approximate exponential decay, $E_{ac}(\Delta)/E^0_{ac} = e^{-\Delta/\Delta_0}$. Figure 6 also shows that the attenuation computed in the 3D model is captured fairly well by the 1D model, including good quantitative agreement within 7% between the estimated characteristic length scale Δ_0 in the 1D and 3D models, respectively.

IV. ACOUSTOPHORETIC BULK DEVICES

We now move on to the second type of acoustofluidic devices, namely, the bulk silicon-glass devices used in many lab-on-a-chip applications as reviewed by Lenshof *et al.*[37] As sketched in Fig. 1(b), these devices consist of a silicon-glass-based acoustofluidic chip coupled to a bulk PZT transducer. In contrast to the capillary-tube devices, the manipulation of the particles in the silicon-glass chip relies on horizontal half-wave pressure resonances. Because the pressure half-wave is anti-symmetric around the vertical center plane of the channel, the symmetric motion actuated by a usual PZT transducer must be broken. This is normally done geometrically by placing the transducer off-center[9,15,38] or splitting the top electrode of the transducer and actuated it by an anti-symmetric voltage actuation.[27,39] The symmetry breaking could also be achieved by incorporating side walls with different angles or curvatures. In this work, we use the first method and displace the silicon-glass chip by $y_0 = 1$ mm with respect to the (xz)-mirror-plane of the PZT transducer; see Fig. 7.

A. Coupling layer analysis in 2D

It is well known that even with an ideal long straight channel in such devices, axial variations and acoustic hot spots appear along the channel.[40] However, when studying a region in the channel near a local maximum in the acoustic field where the axial gradients are vanishing small, 2D models describe the acoustic fields very well.[15,40] In this

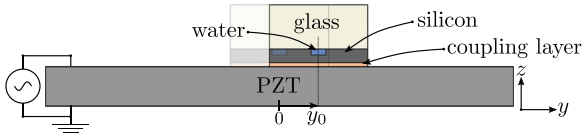

FIG. 7. (Color online) Cross section in the vertical yz-plane of the silicon-glass device in Fig. 1(b), showing the PZT transducer, coupling layer, and silicon-glass chip with the microchannel (blue). The chip is displaced from the PZT center plane by $y_0 = 1$ mm. The sketch defines the 2D model; see Table V.

analysis, we, therefore, study the silicon-glass device in a 2D model as shown in Fig. 7. As introduced in Sec. II, the PZT transducer is a z-polarized Meggitt-Pz26 transducer (Meggitt A/S, Kvistgaard, Denmark) but now with a thickness of 1000 μm with a resonance mode near 2 MHz. The materials and dimensions used in the silicon-glass-device simulations are listed in Tables III and V, respectively.

The coupling layer analysis is analogous to the one in Sec. III. The acoustic resonances are located as peaks in the acoustic energy density spectrum $E_{ac}(f)$ in the frequency range 1.5–2.5 MHz as a function of the coupling material (glycerol or epoxy) and layer thickness Δ from 0 to 100 μm.

Similar to Fig. 4, in Fig. 8(a), we show a scatterplot in which the points represent resonances at the frequency f_{res} for a coupling layer of thickness Δ in the range from 0 to 100 μm with point areas proportional to E_{ac}/E^0_{ac}. Multiple resonances are identified, however, the resonance at $f_{res} = 1.940$ MHz stands out with E^0_{ac} being more than 60 times larger than any other zero-layer peak. The frequency of this resonance is nearly independent of the coupling material and layer thickness Δ. However, in Fig. 8(b), we see a fundamental difference between the two coupling materials: For glycerol, the normalized acoustic energy density E_{ac}/E^0_{ac} decreases by one order of magnitude at a length scale ~100 nm, whereas for epoxy, E_{ac}/E^0_{ac} stays nearly constant up to $\Delta \sim 1$ μm, followed by a slow drop to 0.75 at $\Delta = 10$ μm and 0.2 at $\Delta \sim 50$ μm. This behavior may be explained by the geometry of the acoustics and fundamental mechanical difference between elastic solids and viscous fluids. In the silicon-glass device, the direction of the standing pressure half-wave is orthogonal to the transducer polarization, and to excite this resonance mode, the transmission of shear waves from the transducer to the microchannel is required. However, only a solid coupling layer and not a viscous fluid can support such a transmission of shear waves.

TABLE V. The width (W) and height (H) of the silicon base (si), glass cover (gl), channel (ch), PZT transducer (pzt), and silver electrodes (el); see Fig. 7.

Symbol	Value	Symbol	Value
W_{si}	2520 μm	H_{si}	350 μm
W_{gl}	2520 μm	H_{gl}	1130 μm
W_{ch}	377 μm	H_{ch}	157 μm
W_{pzt}	12 000 μm	H_{pzt}	982 μm
W_{el}	12 000 μm	H_{el}	9 μm

https://doi.org/10.1121/10.0004871

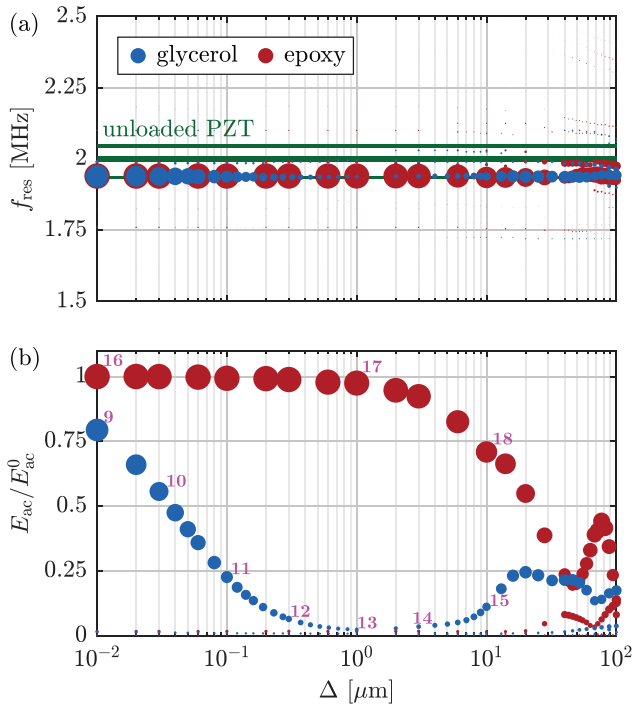

FIG. 8. (Color online) Scatter plots with point areas proportional to E_{ac}/E^0_{ac} of responses to the increasing coupling-layer thickness Δ simulated in the 2D model of the silicon-glass device. (a) Resonance frequencies f_{res} and (b) normalized acoustic energy density E_{ac}/E^0_{ac} are shown. Animated gif-files of the ten modes enumerated 9–18 (magenta numbers) are given in the supplementary material (Ref. 36).

In Fig. 8(b), we have selected ten 2D resonance modes enumerated 9–18 (magenta numbers). For each of these modes, we have computed an animated gif-file, given in the supplementary material,[36] that shows the temporal behavior. When studying the morphology of the modes through the animated gif-files, we find that the morphology of the sustained mode 16 without a coupling layer, $\Delta = 0$ μm, is maintained as a solid epoxy coupling layer of increasing thickness Δ is introduced, so mode 16 $\simeq$ mode 17 $\simeq$ mode 18. In contrast, the evolution of the attenuated mode 9 without a coupling layer, $\Delta = 0$ μm, is more complex. For mode 9, the vertical displacement u_z along the top of the microchannel is nearly anti-symmetric. As a fluid glycerol coupling layer of increasing thickness Δ is introduced, the symmetry of u_z evolves through modes 10, 11, and 12 to become nearly symmetric for mode 13 with $\Delta = 1$ μm. At the same time, the horizontal displacement u_y, which undergoes a nearly full wave oscillation along the vertical edges $y = \pm\frac{1}{2}W_{gl}$ of the chip, changes from having nodes at the top and bottom of the chip to having anti-nodes. This morphology is maintained for a further increase in Δ, so mode 13 $\simeq$ mode 14 $\simeq$ mode 15. In the following analysis, valid for very thin coupling layers, $\Delta \ll 0.1$ mm, we can explain the weakening of the resonance strength going from mode 9 to mode 13, but not the regaining of strength that sets in for the thicker coupling layer going from mode 13 to mode 15.

B. Dissipation in the glycerol coupling layer

The critical glycerol coupling-layer thickness $\Delta_{crit} = 100$ nm, observed in Fig. 8(b), requires a physical explanation as this length scales is far from any of the geometrical sizes or acoustic wavelengths in the system. The small thickness $\Delta < 0.1$ mm of the coupling layer implies large shear strain rates and a large amount of viscous dissipation. We assume that Δ_{crit} is the coupling-layer thickness, where the time-averaged viscous dissipation power $\langle P^{visc}_{crit}\rangle$ in the glycerol coupling layer equals the time-averaged acoustic power $\langle P_{ac}\rangle$ delivered to the half-wave pressure resonator. For an ideal resonator of length L_{ch}, width W_{ch}, height H_{ch}, average acoustic energy density E_{ac}, and quality factor Q, together with a coupling layer of thickness Δ_{crit}, width $W_{glc} = W_{gl}$, and dynamic viscosity η_{glc}, we obtain

$$\langle P_{ac}\rangle = \langle P^{visc}_{crit}\rangle, \tag{17a}$$

$$\langle P_{ac}\rangle = \int \langle p_1 \boldsymbol{v}_1 \cdot \boldsymbol{n}\rangle \, dA = \frac{16\pi}{Q} c_0 E_{ac} H_{ch} L_{ch}, \tag{17b}$$

$$\langle P^{visc}_{crit}\rangle = \int \langle \boldsymbol{\nabla} \boldsymbol{v}_1 : \boldsymbol{\tau}\rangle \, dV \approx \frac{4\pi^2 \eta_{glc} E_{ac}}{Q^2 \rho_0 \Delta_{crit}} W_{glc} L_{ch}. \tag{17c}$$

Solving for Δ_{crit}, we obtain

$$\Delta_{crit} = \frac{\pi \eta_{glc} W_{glc}}{4 Q \rho_0 c_0} H_{ch}. \tag{18}$$

The effect of the surrounding silicon-glass chip is included in the quality factor $Q = f_{res}/\Delta f$, found from the resulting full-width Δf at half maximum of the corresponding resonance peak $E_{ac}(f)$ at the resonance frequency f_{res}. The estimate for Δ_{crit} is validated numerically by varying the material and geometrical parameters in Eq. (18). The chosen material and geometric variations are listed in Table VI together with the resulting critical thickness Δ_{crit} and quality factor Q. Using the 2D model, the acoustic energy density E_{ac} is simulated, and the result is normalized by E^0_{ac}, which is the value without a coupling layer. In Fig. 9, the simulated

TABLE VI. 2D simulations of the critical coupling-layer thickness Δ_{crit} and quality factor Q for the standard configuration c0 defined in Fig. 7 and Tables III–V with a coupling layer of viscosity $\eta^0_{glc} = 1.137$ Pa s and width $W^0_{gl} = 2520$ μm, and a microchannel of height $H^0_{ch} = 157$ μm, containing a fluid of density $\rho^0_0 = 997.05$ kg m^{-3}. Eight other configurations c1–c8 are obtained from c0 by changing one of the four parameter values as listed.

Configuration	$\frac{\eta_{glc}}{\eta^0_{glc}}$	$\frac{\rho_0}{\rho^0_0}$	$\frac{H_{ch}}{H^0_{ch}}$	$\frac{W_{gl}}{W^0_{gl}}$	Δ_{crit} (nm)	Q
c0	1.0	1.0	1.0	1.0	68.5	140
c1	0.05	1.0	1.0	1.0	3.4	140
c2	0.1	1.0	1.0	1.0	6.9	140
c3	0.2	1.0	1.0	1.0	13.7	140
c4	0.5	1.0	1.0	1.0	34.3	140
c5	2.0	1.0	1.0	1.0	137.0	140
c6	1.0	2.0	1.0	1.0	73.0	140
c7	1.0	1.0	0.5	1.0	202.2	95
c8	1.0	1.0	1.0	0.5	38.5	125

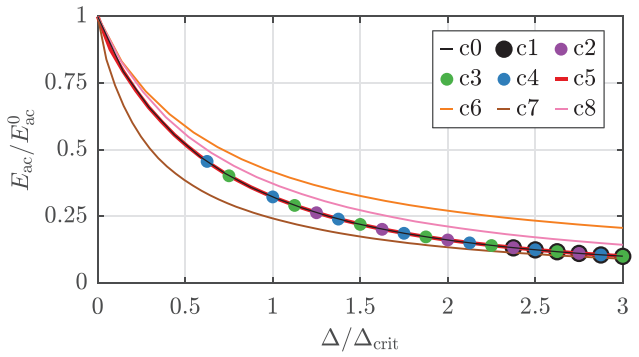

FIG. 9. (Color online) Simulated normalized acoustic energy density E_{ac}/E^0_{ac} versus the normalized coupling-layer thickness Δ/Δ_{crit} for the nine different system configurations $c0$–$c8$ listed in Table VI.

ratio E_{ac}/E^0_{ac} is plotted versus the normalized coupling-layer thickness Δ/Δ_{crit}, and for the wide range of parameters, it is seen that, indeed, E_{ac}/E^0_{ac} decays on the critical coupling-layer thickness scale Δ_{crit}.

The obtained values for Q listed in Table VI range from 95 to 140, which is in line with values reported in the literature: For a acoustofluidic device with a thin glycerol layer with unspecified thickness, Barnkob *et al.* measured $Q = 209$ for one main resonance,[9] and in their thorough 3D analysis of the dissipation in the various parts of an acoustofluidic device with a 20-μm-thick epoxy coupling layer, Hahn and Dual computed $Q = 166$ and found that 40% of the loss per cycle was due to the epoxy layer.[4]

V. CONCLUSION

We have developed a numerical 3D model to study the role of coupling layers in acoustofluidic devices. The model includes the PZT transducer with electrodes, coupling layer, and acoustofluidic chip with the fluid-filled microchannel. The model is used to study two well-known types of acoustofluidic devices: a glass capillary tube and silicon-glass chip, classified as vertical and horizontal resonators, respectively, relative to the polarization axis of the transducer. For each device, a viscous glycerol and solid epoxy coupling layer was studied.

For vertical resonators, such as the capillary-tube device, we have found that for a given zero-layer resonance, the coupling layer can either result in a sustaining or attenuating resonance. We have established the criterion [Eq. (10)] to predict which of the two behaviors will occur, based on a relation involving the phase of the acoustic wave. For the attenuated waves, we have derived expression (27) to estimate the characteristic layer thickness Δ_0 at which the resonance is attenuated. The computed values for Δ_0, as shown in Fig. 6, are between 10 and 25 μm, which demonstrates the direct relevance of our analysis for glass-capillary-tube experiments, because the measured coupling-layer thickness Δ is reported in the literature to lie in the range from 5 to 20 μm.[6,7,28–31]

For horizontal resonators, such as the silicon-glass device, the acoustic resonances are partially powered by the shear-wave transmission through the coupling layer. For the device with an epoxy coupling layer, the slow weakening of the sustained resonance mode 16 of Fig. 8(b), which sets in at a layer thickness around 10 μm for mode 18, also happens at the experimentally relevant length scale given above. However, for the device with a glycerol coupling layer that cannot sustain shear waves, the coupling layer works as a strongly dissipative element that suppresses the resonance. For this case, a critical viscous dissipation thickness Δ_{crit} was presented in Eq. (18), based on scaling arguments in a 1D two-component model. All of the computed values for Δ_{crit} listed in Table VI are smaller than 0.2 μm, which is apparently much smaller than the experimentally relevant layer thickness. Nevertheless, the expression for Δ_{crit} and its numerical verification in Fig. 9 elucidate the physical mechanism from a theoretical point of view, although this regime may be difficult to access experimentally. How thin a glycerol layer can be in an acoustofluidic experiment is not known to us. In many research papers, where such layers are used, they are just stated to be thin without being assigned a measured value.

The simulation results presented have led to the formulation of design rules for choosing an optimal coupling layer between the PZT transducer and acoustofluidic device. The design rules involve material parameters, geometrical parameters, and information about the orientation of the given acoustic resonance mode relative to the polarization axis of the transducer. We hope that these rules will prove useful and their limitations will be understood better by experimental validation.

ACKNOWLEDGMENTS

The authors were supported by Independent Research Fund Denmark, Technology and Production Sciences (Grant No. 8022-00285B).

[1]V. T. Rathod, "A review of acoustic impedance matching techniques for piezoelectric sensors and transducers," Sens. **20**(14), 4051 (2020).
[2]M. Hill, Y. Shen, and J. J. Hawkes, "Modelling of layered resonators for ultrasonic separation," Ultrasonics **40**(1-8), 385–392 (2002).
[3]P. Glynne-Jones, R. J. Boltryk, and M. Hill, "Acoustofluidics 9: Modelling and applications of planar resonant devices for acoustic particle manipulation," Lab Chip **12**(8), 1417–1426 (2012).
[4]P. Hahn and J. Dual, "A numerically efficient damping model for acoustic resonances in microfluidic cavities," Phys. Fluids **27**, 062005 (2015).
[5]B. Hammarström, T. Laurell, and J. Nilsson, "Seed particle enabled acoustic trapping of bacteria and nanoparticles in continuous flow systems," Lab Chip **12**, 4296–4304 (2012).
[6]J. Lei, P. Glynne-Jones, and M. Hill, "Acoustic streaming in the transducer plane in ultrasonic particle manipulation devices," Lab Chip **13**(11), 2133–2143 (2013).
[7]P. Mishra, M. Hill, and P. Glynne-Jones, "Deformation of red blood cells using acoustic radiation forces," Biomicrofluidics **8**(3), 034109 (2014).
[8]I. Gralinski, S. Raymond, T. Alan, and A. Neild, "Continuous flow ultrasonic particle trapping in a glass capillary," J. Appl. Phys. **115**(5), 054505 (2014).
[9]R. Barnkob, P. Augustsson, T. Laurell, and H. Bruus, "Measuring the local pressure amplitude in microchannel acoustophoresis," Lab Chip **10**(5), 563–570 (2010).
[10]C. Magnusson, P. Augustsson, A. Lenshof, Y. Ceder, T. Laurell, and H. Lilja, "Clinical-scale cell-surface-marker independent acoustic

microfluidic enrichment of tumor cells from blood," Anal. Chem. **89**(22), 11954–11961 (2017).
[11]K. Petersson, O. Jakobsson, P. Ohlsson, P. Augustsson, S. Scheding, J. Malm, and T. Laurell, "Acoustofluidic hematocrit determination," Anal. Chim. Acta **1000**, 199–204 (2018).
[12]N. R. Skov, J. S. Bach, B. G. Winckelmann, and H. Bruus, "3D modeling of acoustofluidics in a liquid-filled cavity including streaming, viscous boundary layers, surrounding solids, and a piezoelectric transducer," AIMS Math. **4**, 99–111 (2019).
[13]J. S. Bach and H. Bruus, "Theory of pressure acoustics with viscous boundary layers and streaming in curved elastic cavities," J. Acoust. Soc. Am. **144**, 766–784 (2018).
[14]P. B. Muller, R. Barnkob, M. J. H. Jensen, and H. Bruus, "A numerical study of microparticle acoustophoresis driven by acoustic radiation forces and streaming-induced drag forces," Lab Chip **12**, 4617–4627 (2012).
[15]P. B. Muller, M. Rossi, A. G. Marin, R. Barnkob, P. Augustsson, T. Laurell, C. J. Kähler, and H. Bruus, "Ultrasound-induced acoustophoretic motion of microparticles in three dimensions," Phys. Rev. E **88**(2), 023006 (2013).
[16]A. Bermúdez, L. Hervella-Nieto, A. Prieto, and R. Rodríguez, "An optimal perfectly matched layer with unbounded absorbing function for time-harmonic acoustic scattering problems," J. Comput. Phys. **223**(2), 469–488 (2007).
[17]COMSOL Multiphysics 5.5 (2019), available at http://www.comsol.com (Last viewed 13 April 2021).
[18]M. W. H. Ley and H. Bruus, "Three-dimensional numerical modeling of acoustic trapping in glass capillaries," Phys. Rev. Appl. **8**, 024020 (2017).
[19]P. B. Muller and H. Bruus, "Numerical study of thermoviscous effects in ultrasound-induced acoustic streaming in microchannels," Phys. Rev. E **90**(4), 043016 (2014).
[20]CORNING, "Glass silicon constraint substrates" (Corning, Houghton Park C-8, Corning, NY), available at http://www.valleydesign.com/Datasheets/Corning%20Pyrex%207740.pdf (Last viewed 13 April 2021).
[21]AZoMaterials, "Silver—Applications and properties of silver" (AzoMaterials, Manchester, UK, available at https://www.azom.com/properties.aspx?ArticleID=600 (Last viewed 13 April 2021).
[22]M. A. Hopcroft, W. D. Nix, and T. W. Kenny, "What is the Young's modulus of silicon?," J. Microelectromech. Syst **19**, 229–238 (2010).
[23]Meggitt A/S, "Ferroperm matrix data" (Meggitt A/S, Kvistgaard, Denmark), available at https://www.meggittferroperm.com/materials/ (Last viewed 13 April 2021).
[24]J. J. Hawkes and W. T. Coakley, "Force field particle filter, combining ultrasound standing waves and laminar flow," Sens. Actuators, B **75**(3), 213–222 (2001).
[25]B. Hammarström, M. Evander, H. Barbeau, M. Bruzelius, J. Larsson, T. Laurell, and J. Nillsson, "Non-contact acoustic cell trapping in disposable glass capillaries," Lab Chip **10**(17), 2251–2257 (2010).
[26]P. Ohlsson, M. Evander, K. Petersson, L. Mellhammar, A. Lehmusvuori, U. Karhunen, M. Soikkeli, T. Seppa, E. Tuunainen, A. Spangar, P. von Lode, K. Rantakokko-Jalava, G. Otto, S. Scheding, T. Soukka, S. Wittfooth, and T. Laurell, "Integrated acoustic separation, enrichment, and microchip polymerase chain reaction detection of bacteria from blood for rapid sepsis diagnostics," Anal. Chem. **88**(19), 9403–9411 (2016).
[27]W. N. Bodé, L. Jiang, T. Laurell, and H. Bruus, "Microparticle acoustophoresis in aluminum-based acoustofluidic devices with PDMS covers," Micromachines **11**(3), 292 (2020).
[28]P. Hahn, O. Schwab, and J. Dual, "Modeling and optimization of acoustofluidic micro-devices," Lab Chip **14**, 3937–3948 (2014).
[29]R. J. Townsend, M. Hill, N. R. Harris, and M. B. McDonnell, "Performance of a quarter-wavelength particle concentrator," Ultrasonics **48**(6-7), 515–520 (2008).
[30]A. Lamprecht, S. Lakamper, T. Baasch, I. A. T. Schaap, and J. Dual, "Imaging the position-dependent 3D force on microbeads subjected to acoustic radiation forces and streaming," Lab Chip **16**, 2682–2693 (2016).
[31]V. Pereno, M. Aron, O. Vince, C. Mannaris, A. Seth, M. de Saint Victor, G. Lajoinie, M. Versluis, C. Coussios, D. Carugo, and E. Stride, "Layered acoustofluidic resonators for the simultaneous optical and acoustic characterisation of cavitation dynamics, microstreaming, and biological effects," Biomicrofluidics **12**(3), 034109 (2018).
[32]W. Slie, A. Donfor, Jr., and T. Litovitz, "Ultrasonic shear and longitudinal measurements in aqueous glycerol," J. Chem. Phys. **44**(10), 3712–3718 (1966).
[33]L. Negadi, B. Feddal-Benabed, I. Bahadur, J. Saab, M. Zaoui-Djelloul-Daouadji, D. Ramjugernath, and A. Negadi, "Effect of temperature on density, sound velocity, and their derived properties for the binary systems glycerol with water or alcohols," J. Chem. Thermodyn. **109**, 124–136 (2017).
[34]N.-S. Cheng, "Formula for the viscosity of a glycerol-water mixture," Ind. Eng. Chem. Res. **47**(9), 3285–3288 (2008).
[35]I. I. Perepechko, V. A. Danilov, and V. V. Nizhegorodov, "Ultrasonic velocity in epoxy resin at temperatures down to 4.2 K," Mech. Compos. Mater. **32**, 316–320 (1996).
[36]See supplementary material https://www.scitation.org/doi/suppl/10.1121/10.0004871 for details on the 18 resonance modes enumerated 1–18 in Figs. 4 and 8, as well as an animated gif-file of each of these modes.
[37]A. Lenshof, C. Magnusson, and T. Laurell, "Acoustofluidics 8: Applications in acoustophoresis in continuous flow microsystems," Lab Chip **12**, 1210–1223 (2012).
[38]A. Tahmasebipour, L. Friedrich, M. Begley, H. Bruus, and C. Meinhart, "Toward optimal acoustophoretic microparticle manipulation by exploiting asymmetry," J. Acoust. Soc. Am. **148**(1), 359–373 (2020).
[39]R. P. Moiseyenko and H. Bruus, "Whole-system ultrasound resonances as the basis for acoustophoresis in all-polymer microfluidic devices," Phys. Rev. Appl. **11**, 014014 (2019).
[40]P. Augustsson, R. Barnkob, S. T. Wereley, H. Bruus, and T. Laurell, "Automated and temperature-controlled micro-PIV measurements enabling long-term-stable microchannel acoustophoresis characterization," Lab Chip **11**(24), 4152–4164 (2011).